Ceramics International 49 (2023) 10298–10304

Contents lists available at ScienceDirect

Ceramics International

journal homepage: www.elsevier.com/locate/ceramint

Tunability of magnetoelectric coupling in perovskite/spinel-based triphasic multiferroic composites for multistate devices

Abdul Ghaffar [a], Mariam Fatima [a], Ghulam M. Mustafa [b,*], Syed Anas Hafeez [a], Asif Mahmood [c], Shahid Atiq [a,**]

[a] Centre of Excellence in Solid State Physics, University of the Punjab, Lahore, 54590, Pakistan
[b] Department of Physics, Division of Science and Technology, University of Education, Lahore, Punjab, 54770, Pakistan
[c] Chemical Engineering Department, College of Engineering, King Saud University (KSU), Riyadh, Saudi Arabia

ARTICLE INFO

Keywords:
Multiferoic composites
Triphasic
Perovskite/spinel
X-ray diffraction
Energy density
Magneto-electric effect

ABSTRACT

Multiferroic composites offer a keen interest to researchers because of their huge compositional range, structural flexibility, and their suitability for multifunctional devices. In this regard, we present a series of triphasic perovskite/spinel composites with general formula $0.8[(1–x)SrCoO_{2.29}+ xCr_2FeO_4] + 0.2\ Pb(Zr_{0.58}Ti_{0.42})O_3$ (x = 0.0, 0.33, 0.66 and 1.0) by sol–gel auto-combustion and solid-state approach. The presence of individual crystalline phases of $SrCoO_{2.29}$, Cr_2FeO_4, and $Pb(Zr_{0.58}Ti_{0.42})O_3$ was verified using diffraction data. Morphological investigations demonstrate a homogenous distribution of particles with considerable porosity and particle size in the range of 250–450 nm. The presence and variation of constituent elements in the composition according to their stoichiometric formula were confirmed using energy dispersive X-ray analysis. The energy storage capability was mapped by analyzing the P–E hysteresis loops which gave the measure of saturation and remanent polarizations. These polarizations led to determining the recoverable energy density and energy loss density which highlighted the capacity of these materials for energy storage devices. The increasing magnetic response of the composites with increasing Cr_2FeO_4 contents highlight the indication of improvement in magnetoelectric coupling. In addition, the detection of magnetic field-induced polarization revealed the potential of these materials for magnetic sensors, energy storage, and multistate devices.

1. Introduction

Advancement in the electronic industry is coupled with the discovery of smart functional materials which provides a unique opportunity to develop novel components of devices capable to sense environmental changes such as humidity, temperature, electric and magnetic fields. Recently, ferroelectric and ferromagnetic materials have been utilized separately in various practical fields however, the combination of these mutually exclusive ferroic orders give birth to a new class of materials called magnetoelectric materials [1–3]. Magnetoelectric (ME) coupling in multiferroic materials opens a wide range of possibilities for creating ultra-fast, low-power, and miniaturized novel devices including energy harvesters, sensors, spintronic, and data storage devices [2,3]. Because of the intrinsic incompatibility of ferroelectricity and ferromagnetism, single-phase multiferroics are very rare in nature [4]. In single-phase multiferroics, the ME coupling is weak and exists below room temperature (RT) [5,6]. Hence, the key problem in the development of multiferroics lies in combined ferroelectric and magnetic orders with enhanced coupling between them particularly regarding ambient temperatures [7]. Thus, to achieve a substantial ME coupling in single-phase materials, various studies have been conducted in the past. Therefore, multiferroic composites have vast room available where the ME coupling can be enhanced through strain mediation between ferroelectric and ferromagnetic phases and can improve the operating temperature domain which is essential for practical appliances [8–10]. When a magnetic field is applied to the composites, it changes the particle's shape due to magnetostriction, which passes into the ferroelectric phase. This magnetostriction induces voltage by generating some extra charges owing to the piezoelectric action in the composites [3,11,12]. The interfacial strain that exists between the different phases has a substantial effect on the performance and functionality of the multiferroic composites. A lot of research is currently underway to find materials

* Corresponding author.
** Corresponding author.
E-mail addresses: ghulam.phd.cssp@pu.edu.pk (G.M. Mustafa), satiq.cssp@pu.edu.pk (S. Atiq).

https://doi.org/10.1016/j.ceramint.2022.11.210
Received 1 August 2022; Received in revised form 3 November 2022; Accepted 16 November 2022
Available online 19 November 2022

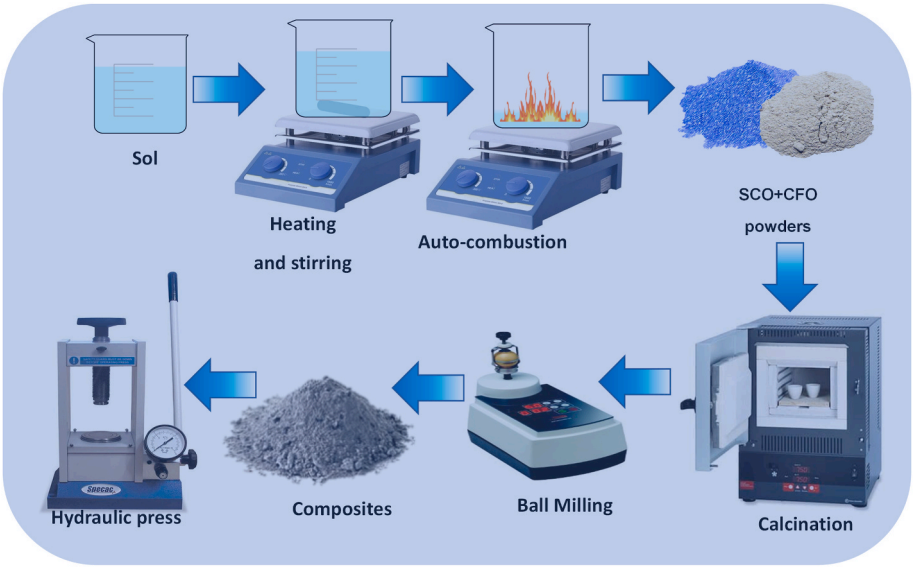

Fig. 1. Pictorial representation of synthesis summary of tri-phase composites.

with a strong ME effect at ambient temperature [4,11,13].

Perovskite-spinel composites have received a lot of attention because of the strain coupling caused by their lattice discrepancy at the boundary. In these composites, the perovskite-phase acts as a piezoelectric and the spinel phase as a magnetostrictive phase [3,11]. Several studies have been conducted in the recent past where different spinel ferro/ferrimagnetic materials ($CoFe_2O_4$, $BiFeO_3$, $MnFe_2O_4$, and $NiFe_2O_4$), were mixed with perovskite ferroelectric materials ($PbZrO_3$, $PbTiO_3$, and $BaTiO_3$), to boost their multiferroic properties [11,14–16]. As compared to bi-phase composites, triphasic composites received more attention because the addition of a third component generated a high value of dielectric constant, especially at the nanoscale [17].

Researchers across the globe devoted a lot of attention to the bi-phase and triphasic composites of $CoFe_2O_4$, $CuFe_2O_4$, and $CrFe_2O_4$ with $BiFeO_3$ (BFO), $Pb(Zr_{0.58}Ti_{0.42})O_3$, and $BaTiO_3$ to enhance the multiferroic characteristics using various chemical routes. For instance, Kumar et al. used the sol–gel method to prepare spinel-perovskite composites of CFO and BFO to analyze ME characteristics. The detection of ME signals was confirmed by magnetocapacitance in the prepared samples [13]. In addition, the fabrication of triphasic ME-composites was published by Jadhav et al., and effectively exhibited the increase in ME coupling caused by the increase in magnetization [18]. Besides these, Moharana et al. synthesized BFO-based triphasic polymer composite in the form of thin film which demonstrated low dielectric loss with a high value of dielectric constant (i.e., 69) [19]. Furthermore, Umair et al. synthesized triphasic composites comprising $BiFeO_3$, Fe_3O_4, and Cr_2O_3 using a sol–gel auto-combustion approach and noticed a remarkable improvement in ME coupling [20]. Recently, considerable work is devoted to improving the ME coupling of triphasic composites in bulk and thin film form. Spinel-perovskite composites in bulk form offer a higher degree of freedom than thin films, allowing them to couple ferroelectric and ferromagnetic phases more strongly at the nanoscale which leads to enhancing the ME effect [14].

Here we synthesized a triphasic composite consisting of chromium ferrite Cr_2FeO_4 (CFO), $CoSrO_3$ (CSO), and lead zirconate titanate $Pb(Zr_{0.58}Ti_{0.42})O_3$ (PZT). In this composite, CFO with spinel structure and *Fd-3m* space-group is a ferrimagnetic material having a lattice constant of 8.378 Å, and magnetic moment of 5.6 μ_B, which is greater than the magnetic moment of FO i.e., 4.0 μ_B [21]. It is revealed by an analytical study of the cation distribution of Cr_2FeO_4 that it has Fe^{2+} and Cr^{3+} at the octahedral site and Fe^{3+} at the tetrahedral site [22]. Across the visible wavelength range, Cr_2FeO_4 is photoconductive which also makes this material attractive for photoelectrochemical applications [23]. After Cr_2FeO_4, the second most important component is strontium cobalt oxide, $SrCoO_{2.29}$ (SCO) which has been employed in functional devices such as electrochemical catalysts and solid fuel cells [24,25]. The SCO has a cubic perovskite structure with a lattice constant of 3.840 Å and Curie temperature (T_C) 305 K. PZT has rhombohedral crystal structure with space group R3c and lattice parameters 4.070 Å. It has excellent piezoelectric properties because of its high spontaneous polarization (P_s) 26.79 μC/cm^2 and Curie temperature (T_c) 508 K and can be used for micro-electromechanical systems (MEMS), vibration damping and microfluidic device applications [26]. In its ground state, SCO has a hole in the O-2p orbital, making it a negative charge transfer energy material [27]. Afterward, PZT, a piezoceramic material, was added to the 0.8[(1–x)SCO + xCFO] composite to boost up its dielectric characteristics without reducing the system's multiferroic features. The above materials are chemically and mechanically stable, with minimal toxicity, which is essential for commercial applications without compromising environmental safety. Thus in this study, we synthesized an eco-friendly triphasic composite 0.8[(1–x)SCO + xCFO] + 0.2PZT, where x = 0.0, 0.33, 0.66, 1.0, through sol–gel auto-combustion technique, and thoroughly investigated the structural, morphological, ferroelectric and ME characteristics. Furthermore, the suitability of these composites for energy storage and multifunctional devices has also been elaborated.

2. Experimental procedures

In this paper, the perovskite/spinel triphasic composites of the form $0.8[(1–x)\ SrCoO_{2.29} + xCr_2FeO_4] + 0.2PZT$ with x = 0.0, 0.33, 0.66 and 1.0 were prepared through a simple sol–gel followed by auto-combustion and ball-milling route. Initially, the sol–gel auto-combustion approach was used to synthesize pure $SrCoO_{2.29}$ and Cr_2FeO_4 samples. The stoichiometric quantities of metal nitrates like strontium nitrate [$Sr(NO_3)_2$; purity ≥98%], cobalt nitrate [$Co(NO_3)_2.6H_2O$; purity ≥98%], chromium nitrate $Cr(NO_3)_3.9H_2O$; purity ≥98%] and iron nitrate [$Fe(NO_3)_3.9H_2O$; purity ≥98%] were utilized as precursors. The schematic diagram of the synthesis of composites is shown in Fig. 1. Urea [CH_4N_2O] and glycine [$C_2H_5NO_2$] have been employed as fuel agents by adjusting their ratio with precursors as 2:1. The solutions of all precursors and fuel agents were mixed and placed on the hotplate at 100 °C for 2 h with continuous stirring. Just after the gel was formed, the temperature was gradually increased to 240 °C to

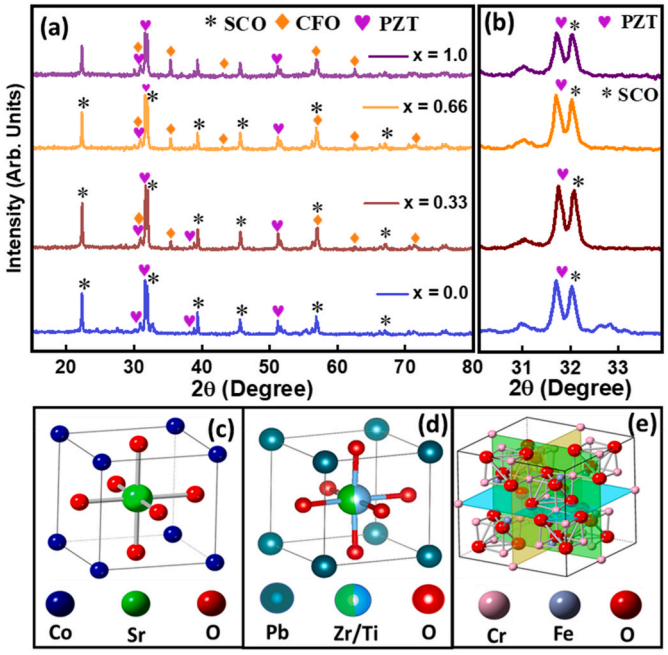

Fig. 2. (a) XRD patterns in 2θ range of 15–80°, and (b) magnified version in 2θ range of 30–34° of tri-phase composites, (c) unit cell of $SrCoO_{2.29}$, (d) unit cell of $PbZr_{0.58}Ti_{0.42}O_3$ and (e) unit cell of Cr_2FeO_4.

trigger the auto-combustion process. Using a mortar and pestle, the residual ash was ground into fine powder. By following the same scheme pure $SrCoO_{2.29}$ and Cr_2FeO_4 were calcined for 3 h in a muffle furnace at 600 °C.

By following the solid-state technique, the PZT was synthesized by combining lead oxide (PbO), zirconium oxide (ZrO_2), and titanium oxide (TiO_2) in a stoichiometric ratio. All these oxides were mixed for 6–7 h in a ball milling chamber at 25 Hz followed by calcination at 1300 °C which resulted in the formation of PZT powder. To prepare the final product, already synthesized $SrCoO_{2.29}$, Cr_2FeO_4, and PZT were further mixed for 2 h at 25 Hz in a ball milling chamber. This mixture was pressed into cylindrical pellets with 7 mm diameter and 1 mm thickness and sintered for 1 h at 400 °C to eliminate the residual gases.

To investigate the crystal structure of the synthesized samples, Bruker D8 advanced X-ray diffractometer was used and diffracted patterns were recorded in the 2θ range of 15–80°. Whereas the morphological study, Nova NanoSEM 450 recorded the images at 50,000 magnifications. Energy dispersive X-ray spectroscopy was employed to detect and compute the weight percentage of various elements in the triphasic composites. The ME coupling along with the ferroelectric feature is mapped by the precision multiferroic tester of Radiant Technology Ins. (USA).

3. Results and discussion

Fig. 2 (a) shows the indexed XRD patterns of the composites in the 2θ range of 15–80°. The indexing method described by B.D. Cullity was implemented to index the diffracted patterns [28]. The magnified view of XRD patterns in the 2θ range of 30–34° is shown in Fig. 2 (b). The indexing of the diffraction peaks of SCO through the analytical method exposed that the peaks at 22.71°, 32.28°, 39.91°, 45.74°, 57.06°, and 67.08° 2θ values correspond to the planes (100), (110), (111), (200), (211) and (220), respectively, were matched with ICSD reference no. 039–1083 which confirmed the formation of the cubic perovskite structure of SCO [24]. The peaks belonging to the perovskite phase of SCO are distinguished by making them with an asterisk sign (*). The unit cell of SCO is shown in Fig. 2(c). In addition, the peaks located at 2θ values of 30.09°, 35.51°, 57.08°, 62.59°, and 71.11° are marked with miller indices (220), (311), (511), (440), and (620) and were recognized by matching with ICSD reference no. 01-089-2618 which confirmed the presence of cubic spinel structure of Cr_2FeO_4. The peaks belonging to the spinel structure of Cr_2FeO_4 are marked with a diamond symbol (◆) and the arrangement of atoms in the unit cell is presented in Fig. 2(e). There were still some unrecognized peaks that appeared at 2θ values of 21.82°, 30.95°, 31.15°, 38.35°, and 50.21° which belong to the diffracted planes (100), (110), (1$\bar{1}$ 0), (1$\bar{1}$1), and (2$\bar{1}$ 0) and identified by comparing with ICSD reference no. 01-073-2022 and this confirmed the presence of rhombohedral structure of $Pb(Zr_{0.58}Ti_{0.42})O_3$. The peaks of PZT are represented by the symbol (♥) and its unit cell representation is shown in Fig. 2(d). The peaks associated with Cr_2FeO_4 were not detected in the first sample, x = 0, indicating the formation of a two-phase composite. For the composition, x = 0.33, peaks matching the Cr_2FeO_4 phase began to develop, demonstrating the existence of triphasic composites. It has been observed that increasing the content of Cr_2FeO_4 caused a decrease in the intensity of peaks belonging to SCO whereas the intensity of peaks associated with CFO increased which is following the relative percentage of various constituents in the material. The lattice constant and crystallite size were computed using the following relations and are mentioned in Table 1 [28].

Table 1
The calculated values of lattice constant and crystallite size of SCO, CFO and PZT.

Material	Lattice parameter (Å)	Crystallite Size (nm)
$SrCoO_{2.29}$	3.840	43.59
PZT	4.070	40.82
Cr_2FeO_4	8.378	60.33

$$a = \frac{\lambda}{2\,Sin\,\theta}\sqrt{h^2+k^2+l^2} \quad (1)$$

$$\text{Crystallite Size} = \frac{0.9\lambda}{\beta\,Sin\,\theta} \quad (2)$$

Where a is lattice constant, (hkl) are miller indices, λ (Cu $K_\alpha \sim 1.5404$ Å) and θ is the wavelength of incident radiation, and Bragg's angle, respectively, β is full width at half maximum.

The FESEM images of the prepared composites, 0.8[(1–x)SCO + xCFO] + 0.2PZT (x = 0, 0.33, 0.66, 1.0) are captured at 50,000 × and are presented in Fig. 3 (a, b, c, d). These images provide a clear picture of the shape and size of particles, their distribution, and surface texture. For x = 0.0, the particles of bi-phase composites have vast variations in size and particle distribution. The size of particles was measured by ImageJ software. It has been observed that most of the particles were in the range of 250–460 nm for x = 0.0. As the CFO is introduced, it reduced the particle size. As the contents of CFO are increased to 0.33, the size of particles is decreased with the increase in particle distribution. In this composition, the average particle size was noticed as 250 nm. The grains of two types were found in the composites: bigger grains of SCO–CFO composites that were manufactured using the sol–gel combustion route, and smaller but denser grains of PZT atoms that were directly mixed into 0.8[(1–x)SCO + xCFO] composites. The agglomeration of tiny grains is responsible for the increase in grain size. For x = 0.66, the agglomeration between particles increased which caused an increase in particle size, however, when SCO is completely replaced with CFO, it significantly reduced the particle's segregation which leads to the reduction in particle size. In this case, the average particle size is noticed as 300 nm. In addition, this composition also has maximum porosity represented by black spaces. The grey area represents the distribution of grains.

For the confirmation of the atomic ratio of constituent elements in the composites, the EDX analysis was performed. Fig. 4(a) presents the energy dispersive X-ray spectra of all compositions [29] while Fig. 4(b)

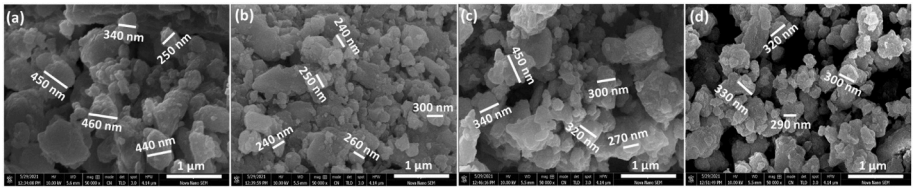

Fig. 3. FESEM images of $0.8[(1\text{-}x)SrCoO_{2.29}+xCr_2FeO_4]+0.2PZT$ for x = (a) 0.0, (b) 0.33, (c) 0.66 and (d) 1.0, at 50,000x

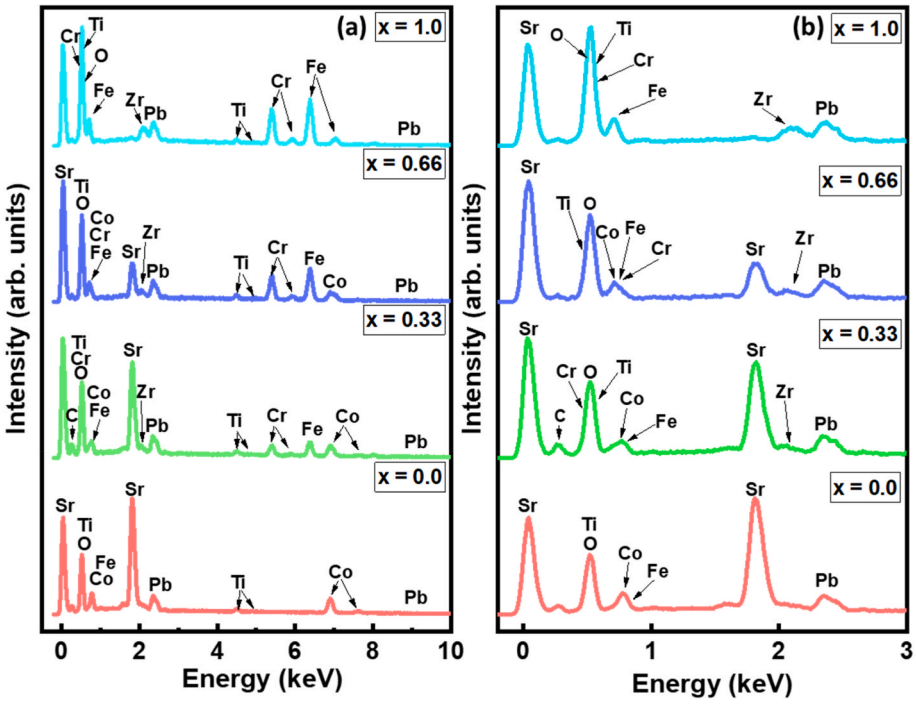

Fig. 4. (a) EDX spectra of $0.8[(1\text{-}x)SrCoO_{2.29}+ xCr_2FeO_4] + 0.2PZT$ (x = 0.0, 0.33, 0.66 and 1.0), and (b) magnified view of lower energy range.

Table 2
Percentage of elements (by weight) in 0.8[(1-x)SCO + x CFO] + 0.2 PZT (x = 0.0, 0.33, 0.66 and 1.0) composites.

Sample No.	Substitutional Contents	Weight (%)							
		Sr	Co	O	Cr	Fe	Pb	Zr	Ti
1	x = 0.0	24.84	55.99	9.39	–	–	8.20	–	1.57
2	x = 0.33	22.43	21.27	27.19	4.86	10.51	9.98	2.57	1.19
3	x = 0.66	10.6	8.80	25.75	13.12	27.72	9.87	2.72	1.42
4	x = 1.0	–	–	28.36	19.44	38.70	9.48	2.90	1.12

illustrates the peak's small energy range. For x = 0.0, all elements of SCO and PZT were identified in di-phase composites. As the CFO is introduced, the peaks associated with Co and Fe were also identified, and the intensity of peaks belonging to Fe and Co also improved. In addition to all these elements, the peak corresponding to C is also acknowledged which appeared in the samples due to the organic stitching tape that was utilized to hold the specimen. Peaks of Fe and Cr grow when CFO concentration rises, and the maximum intensity of Fe peaks is seen at x = 1.0. The calculated weight % of all the elements is given in Table 2. To distinguish the particles belonging to different phases present in the triphase composites, a cross sectional SEM image was captured with its corresponding elemental mapping and represent images of different elements are presented in Fig. 5. It is obvious from these images that the grains of PZT are agglomerated, as evident from the images shown in the right bottom part of Fig. 5, whereas the grains of $SrCoO_{2.29}$ and Cr_2FeO_4 are relatively smaller in size and distributed over relatively larger areas of the sample. Thus, the presence of grains related to all phases of the composites is evidence of formation of triphase composites.

The ferroelectric behavior is any material can easily be probed through its PE hysteresis loops [30]. The P–E loops of all samples at RT in the field strength of ±100 kV are presented in Fig. 6(a). It is evident from these loops that polarization increased with the increasing strength of the electric field which highlighted the linear ferroelectric nature of these triphasic composites. It has been observed that polarization initially increased and after getting a maximum value it slightly decreased. The values of maximum polarization (P_{max}), remanent polarization (P_r), and coercive field have been noted from these PE loops and enlisted in Table 3. The value of P_{max} increased with increasing CFO contents and the highest value of P_{max} and P_r are noticed as 1.53×10^{-4} μC/cm^2 and 8.42×10^{-5} μC/cm^2, respectively for x = 1.0. The variation of ferroelectric parameters with varying concentrations of CFO is presented in Fig. 6(b).

To compute the energy storage density, uni-polar P–E loops are illustrated in Fig. 6(c) at a different concentration whereas Fig. 6(d)

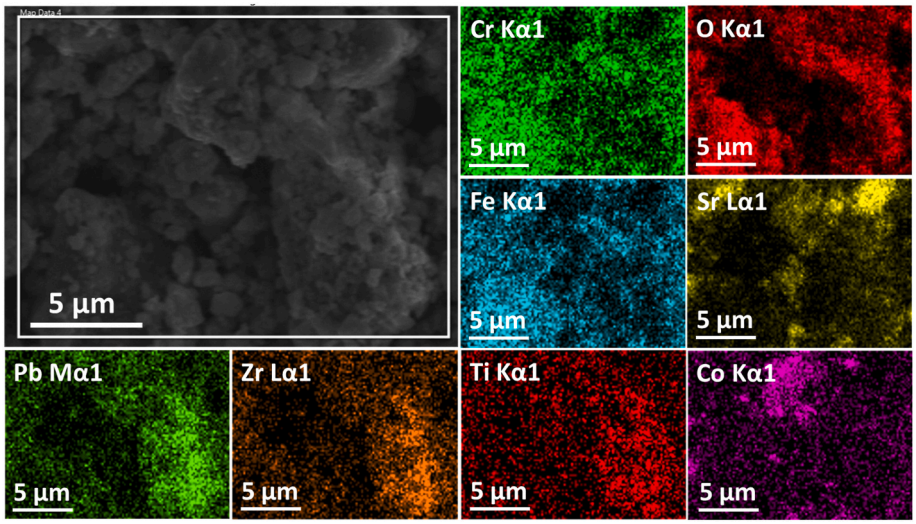

Fig. 5. Elemental mapping of $0.8[(1\text{-}x)SrCoO_{2.29}+ xCr_2FeO_4] + 0.2PZT$ (x = 0.66) composite.

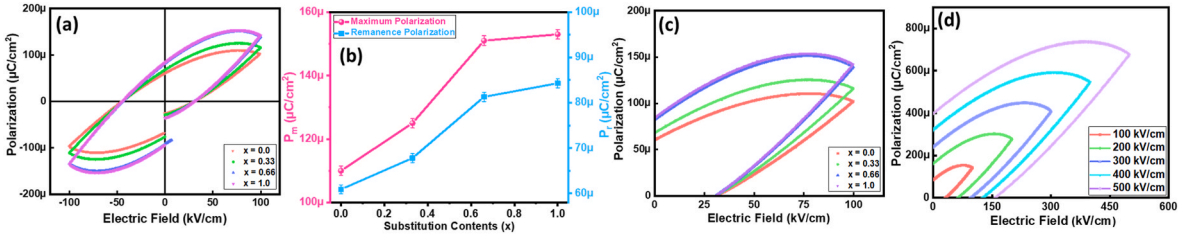

Fig. 6. (a) Polarization versus electric field loops, **(b)** variation of P_m and P_r with substitution contents, **(c)** charge-discharge curves for all compositions and **(d)** charge-discharge curves for x = 1.0 at different field strength.

Table 3
The calculated values of P_m, P_r, E_c, W_R and W_L of $0.8[(1\text{-}x)SCO + x\ CFO] + 0.2$ PZT (x = 0.0, 0.33, 0.66 and 1.0) composites.

Contents	P_m (μC/cm^2)	P_r (μC/cm^2)	E_c (kV/cm)	W_R (mJ/cm^3)	W_L (mJ/cm^3)
x = 0.0	1.10×10^{-4}	6.09×10^{-5}	44.35	10.88×10^{-4}	13.51×10^{-4}
x = 0.33	1.25×10^{-4}	6.78×10^{-5}	44.37	12.68×10^{-4}	15.05×10^{-4}
x = 0.66	1.51×10^{-4}	8.13×10^{-5}	44.38	15.46×10^{-4}	18.04×10^{-4}
x = 1.0	1.53×10^{-4}	8.42×10^{-5}	44.17	15.26×10^{-4}	18.69×10^{-4}

shows the charge-discharge curves for x = 1.0 at different fields strength. These curves help to quantify the recoverable energy density (W_R) and energy loss density (W_L) [31]. The area occupied by P–E loops enumerates the W_L whereas the area trapped by the discharge region and polarization axis gives measures the value of W_R. The values of W_R, W_L, and η can be derived from the calculated values of P_{max}, P_r, and E_c using the following expressions [32]:

$$W_R = \int_{P_r}^{P_m} Edp \tag{3}$$

Where E is the highest applied field, P_m and P_r are the maximum and remanence polarizations. The total energy density (W_T) and W_L are calculated as:

$$W_T = \frac{1}{2} P_{max} E \tag{4}$$

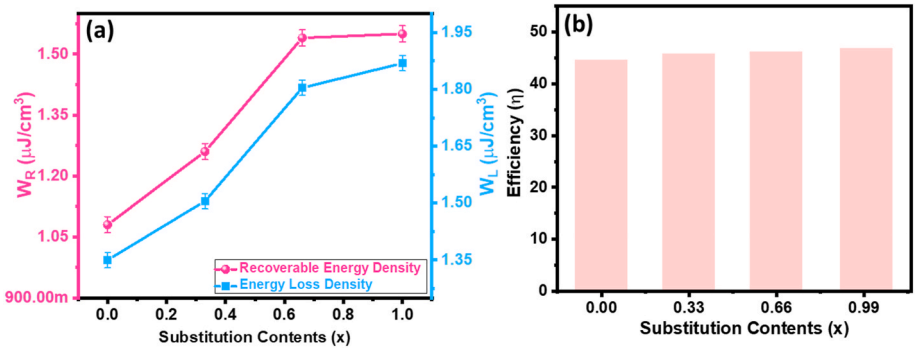

Fig. 7. (a) Variation of recoverable energy density (W_R) and energy loss density (W_L) and **(b)** energy storage efficiency as a function of substitution contents (x).

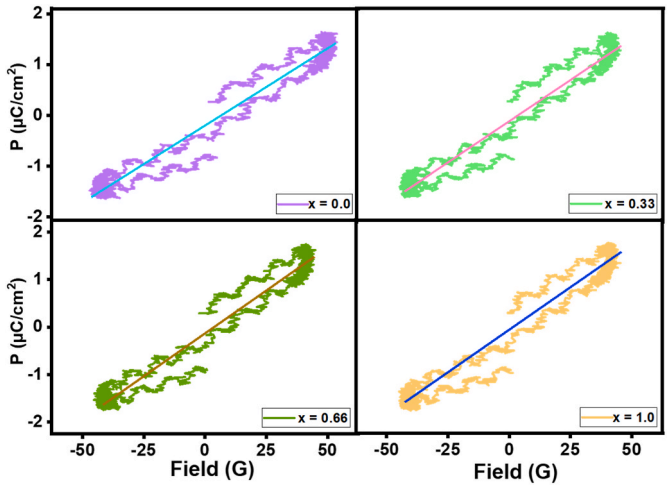

Fig. 8. Polarization versus applied magnetic field for 0.8[(1-x)$SrCoO_{2.29}$+ xCr_2FeO_4] + 0.2PZT (x = 0.0, 0.33, 0.66 and 1.0) composites.

$$W_L = W_T - W_R \tag{5}$$

Table 3 shows the computed values of W_R and W_L, and the variation of W_R and W_L *w.r.t.* substitution contents is drawn in Fig. 7(a). The maximum values of W_R and W_L are found for x = 0.66 and x = 1.0, respectively, as shown in Table 3.

The efficiency of the composites can be calculated using Eq. (6) and the calculated value is presented in Fig. 7(b).

$$\% \eta = \frac{W_R}{W_R + W_L} \times 100 \tag{6}$$

Where η is the efficiency of energy storage.

The ME-coupling effect is a subtle and complex term that explains the induction of electric polarization by a magnetic field and vice versa. It is attributed to the interphase interaction between electric and magnetic phases caused by the elastic contact via strain [33,34]. The underlying phenomenon in this exotic concept of magnetoelectric coupling is piezoelectricity and magnetostriction. The application of electric field modifies the orientation of electric dipoles which induces a strain in ferroelectric material which modifies the interface such that the adjacent ferromagnetic phase perceives that strain and reorients its magnetic dipole moments through magnetostriction. This whole interplay is quantified through a single parameter called the ME coupling coefficient [35]. Fig. 8 presents the ME-coupling effect of the synthesized samples 0.8[(1–x)SCO + xCFO] + 0.2PZT (x = 0.0, 0.33, 0.66, 1.0). It has been demonstrated that polarization varies linearly with the applied magnetic field. The polarity, direction, and strength of the magnetic field, all had a substantial influence on the ME effect. As a result of this linear relationship between P and magnetic field, the prepared composites demonstrate the existence of a notable signal of the ME-coupling coefficient. Because of the significant ME coupling effect, these composites are a good choice for multifunctional devices like MERAMs and magnetic field sensors.

To investigate the magnetic response of these composites, the MH loops are plotted in the range of ±kOe at RT as shown in Fig. 9(a) where it is evident that the parent composition comprising 80% SCO and 20% PZT exhibited with small magnetization which did not meet its saturation level in the provided strength of field and shown as inset. The maximum value of magnetization observed for this composition was 1.138 emu/g at 15 kOe which reduced with the decrease in strength of applied magnetic field and reached to 0.022 emu/g when applied magnetic field was 0 kOe. When 33% CFO was introduced in the composite, the value of magnetization increased and became saturated. The value of saturation magnetization (M_s), remanent magnetization (M_r) and coercive field (H_c) were noticed as 8.763 emu/g, 2.556 emu/g and 632 Oe, respectively for x = 0.33. The value of M_s, M_r and H_c were further increased with the increase in CFO contents. The maximum values of these parameters were recorded for 0.8CFO+0.2PZT composition. The theoretical investigations exhibited the magnetic moment of SCO to be 2.253, 2.254 and 3.882 μ_B using GGA, GGA + SOC and GGA + SOC + U [36]. In another study, Hoffmann et al., showed that the magnetic moment of oxygen deficient and defect free $SrCoO_{3-\delta}$ lies in the range of 2.60–3.19 μ_B [37], whereas the magnetic moment of CFO was reported as 5.6 μ_B [21]. Thus increasing values of M_s, M_r are attributed to the larger value of magnetic moment for CFO as compared to SCO and variation of these parameters with composition is presented in Fig. 9(b) and calculated values in Table 4. This increasing value of magnetization lead to enhance the ME coupling which is required for the advanced multifunctional devices.

4. Conclusion

Here we synthesized a series of triphasic composites 0.8[(1–x) $SrCoO_{2.29}$+ xCr_2FeO_4] + 0.2PZT (x = 0.0, 0.33, 0.66, 1.0) using sol–gel auto-combustion and solid-state method. The analysis of XRD patterns demonstrated the fabrication of composites comprised of three

Table 4
Calculated values of saturation magnetization (M_s), remanent magnetization (M_r) and coercive field (H_c) of 0.8[(1-x)SCO + x CFO] + 0.2 PZT (x = 0.0, 0.33, 0.66 and 1.0) composites.

Contents	M_s (emu/g)	M_r (emu/g)	H_c (Oe)
x = 0.0	1.138	0.022	155
x = 0.33	8.763	2.556	632
x = 0.66	14.869	4.845	679
x = 1.0	29.029	9.560	690

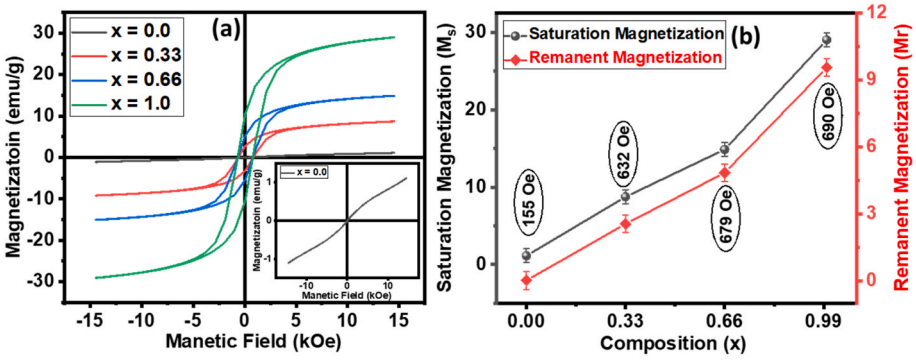

Fig. 9. (a) Magnetization versus magnetic field loops and (b) saturation magnetization, remanent magnetization and coercive field of 0.8[(1-x)$SrCoO_{2.29}$+ xCr_2FeO_4] + 0.2PZT (x = 0.0, 0.33, 0.66 and 1.0) composites.

crystalline phases with no impurity. The observations of FESEM images revealed that the addition of Cr_2FeO_4 homogenized the particle distribution with the reduction of average grain size from 350 nm to 250 nm. The calculation of the weight percent of all constituent elements according to their stoichiometric formula was confirmed from EDX analysis. A distinctive ferroelectric behavior has been seen in the composites, with P_m reaching a maximum value of 1.53×10^{-4} μC/cm^2 for the x = 1.0 specimen. The value of P_r is also increased with the Cr_2FeO_4 substitution, and the highest value of P_r was noticed for x = 1.0 i.e., 8.42×10^{-5} μC/cm^2. The value of W_R is also enhanced by increasing the substitution contents. The significant ME response for all specimens revealed that these composites are suitable for the manufacture of multifunctional devices. Magnetic properties of these tri-phase composites revealed that the value of M_s increased from 1.138 to 29.029 emu/g, M_r 0.022–9.560 emu/g and H_c from 155 to 690 Oe which highlighted the importance of incorporating the magnetic component in the composite and its applicability for futuristic multifunctional devices.

Declaration of competing interest

The authors declare that they have no known competing financial interests or personal relationships that could have appeared to influence the work reported in this paper.

Acknowledgement

The authors would like to acknowledge the Researcher's Supporting Project Number (RSP-2021/43), King Saud University, Riyadh, Saudi Arabia.

References

[1] N.A. Spaldin, Multiferroics beyond electric-field control of magnetism, Proc. Roy. Soc. A 476 (2233) (2020), 20190542.
[2] Y. Wang, J. Li, D. Viehland, Magnetoelectrics for magnetic sensor applications: status, challenges and perspectives, Mater. Today 17 (6) (2014) 269–275.
[3] N.A. Spaldin, S.W. Cheong, R. Ramesh, Multiferroics: past, present, and future, Phys. Today 63 (10) (2010) 38–43.
[4] D.K. Pradhan, S. Kumari, R.K. Vasudevan, S. Dugu, P.T. Das, V.S. Puli, A. Kumar, Room temperature multiferroicity and magnetodielectric coupling in 0–3 composite thin films, J. Appl. Phys. 127 (19) (2020), 194104.
[5] S.W. Cheong, M. Mostovoy, Multiferroics: a magnetic twist for ferroelectricity, Nat. Mater. 6 (1) (2007) 13–20.
[6] Y.H. Chu, L.W. Martin, M.B. Holcomb, R. Ramesh, Controlling magnetism with multiferroics, Mater. Today 10 (10) (2007) 16–23.
[7] A. Jain, Y.G. Wang, N. Wang, Y. Li, F.L. Wang, Tuning the dielectric, ferroelectric and electromechanical properties of $Ba_{0\cdot83}Ca_{0.10}Sr_{0.07}TiO_3$–$MnFe_2O_4$ multiferroic composites, Ceram. Int. 46 (6) (2020) 7576–7585.
[8] Y. Li, Z. Wang, J. Yao, T. Yang, Z. Wang, J.M. Hu, D. Viehland, Magnetoelectric quasi-(0-3) nanocomposite heterostructures, Nat. Commun. 6 (1) (2015) 1–7.
[9] D.K. Pradhan, V.S. Puli, S. Kumari, S. Sahoo, P.T. Das, K. Pradhan, D.K. Pradhan, J. F. Scott, R.S. Katiyar, Studies of phase transitions and magnetoelectric coupling in PFN-CZFO multiferroic composites, J. Phys. Chem. C 120 (3) (2016) 1936–1944.
[10] R. Köferstein, F. Oehler, S.G. Ebbinghaus, Fine-grained magnetoelectric $Sr_{0.5}Ba_{0.5}Nb_2O_6$–$CoFe_2O_4$ composites synthesized by a straightforward one-pot method, Mater. Chem. Phys. 278 (2022), 125616.
[11] Z. Manzoor, A. Khalid, G.M. Mustafa, S.M. Ramay, S. Naseem, S. Atiq, Magnetoelectric coupling caused by strain mediation in hetero-structured spinel-perovskite multiferroic composites, J. Magn. Magn Mater. 500 (2020), 166409.
[12] S.R. Wadgane, S.T. Alone, A. Karim, G. Vats, S.E. Shirsath, R.H. Kadam, Magnetic field induced polarization and magnetoelectric effect in $Na_{0.5}Bi_{0.5}TiO_3$–$Co_{0.75}Zn_{0.25}Cr_{0.2}Fe_{1.8}O_4$ multiferroic composite, J. Magn. Magn Mater. 471 (2019) 388–393.
[13] M. Kumar, K.L. Yadav, Synthesis of nanocrystalline $xCuFe_2O_4$–$(1-x)BiFeO_3$ magnetoelectric composite by chemical method, Mater. Lett. 61 (10) (2007) 2089–2092.
[14] A. Jain, Y.G. Wang, N. Wang, Y. Li, F.L. Wang, Influence of individual phases on the magnetoelectric coupling and electromechanical response in $(1-x)Ba_{0.83}Ca_{0.10}Sr_{0.07}TiO_3$–$xBiFeO_3$ (x= 0–0.30) multiferroic composites, J. Magn. Magn Mater. 495 (2020), 165905.
[15] Y. Qing, L. Ma, X. Hu, F. Luo, W. Zhou, $NiFe_2O_4$ nanoparticles filled $BaTiO_3$ ceramics for high-performance electromagnetic interference shielding applications, Ceram. Int. 44 (7) (2018) 8706–8709.
[16] P. Phansamdaeng, J. Khemprasit, Study on magnetic and dielectric properties of $BaTiO_3/MnCr_{0.\ 2}Fe_{1.8}O_4$ composite material, J. Alloys Compd. 776 (2019) 105–110.
[17] O. Sanches, D.H.F. Kanda, L.F. Malmonge, M.J. da-Silva, W.K. Sakamoto, J. A. Malmonge, Synergistic effects on polyurethane/lead zirconate titanate/carbon black three-phase composites, Polym. Test. 60 (2017) 253–259.
[18] P.A. Jadhav, M.B. Shelar, B.K. Chougule, Magnetoelectric effect in three phase y $(Ni_{0.5}Cu_{0.2}Zn_{0.3}Fe_2O_4) + (1-y)$(50% BaTiO3 + 50% PZT) ME composites, J. Alloys Compd. 479 (1–2) (2009) 385–389.
[19] S. Moharana, T. Yadav, P.A. Alvi, A. Pathak, R.N. Mahaling, Enhanced dielectric and electrical properties of tri-phase percolative PVDF–$BiFeO_3$–Carbon Black (CB) composite film, J. Mater. Sci. Mater. Electron. 32 (5) (2021) 6038–6046.
[20] M. Umair, A. Quader, M. Imran, M.A. Yaqub, S.M. Ramay, S. Atiq, Significant impact of spinel ferrites in evolution of magneto-electric coupling in novel tri-phase composites, Ceram. Int. 48 (10) (2022) 14473–14480.
[21] L.I.U. Jun, L.I.U. Yu, C.X. Meng, D.H. Ning, Electronic structures of new half-metal material $CrFe_2O_4$, Acta Phys. Chim. Sin. 25 (2009) 107–112.
[22] K. Nishamol, K.S. Rahna, S. Sugunan, Selective alkylation of aniline to N-methyl aniline using chromium manganese ferrospinels, J. Mol. Catal. Chem. 209 (1–2) (2004) 89–96.
[23] S.A. Chambers, T.C. Droubay, T.C. Kaspar, I.H. Nayyar, M.E. McBriarty, S. M. Heald, P.V. Sushko, Electronic and optical properties of a semiconducting spinel (Fe_2CrO_4), Adv. Funct. Mater. 27 (9) (2017), 1605040.
[24] L. Troncoso, M.C. Gardey, M.T. Fernández-Díaz, J.A. Alonso, New rhenium-doped $SrCo_{1-x}Re_xO_{3-\delta}$ perovskites performing as cathodes in solid oxide fuel cells, Mater 9 (9) (2016) 717.
[25] N. Li, J. Chen, X. Chen, Y. Lai, C. Yu, L. Yao, Y. Liang, Novel visible-light-driven $SrCoO_3/Ag_3PO_4$ heterojunction with enhanced photocatalytic performance for tetracycline degradation, Environ. Sci. Pollut. R. 29 (7) (2022) 9693–9706.
[26] K.T. Arul, M.R. Rao, Ferroelectric properties of flexible PZT composite films, J. Phys. Chem. Solid. 146 (2020), 109371.
[27] J. Kuneš, V. Křápek, N. Parragh, G. Sangiovanni, A. Toschi, A.V. Kozhevnikov, Spin state of negative charge-transfer material $SrCoO_3$, Phys. Rev. Lett. 109 (11) (2012), 117206.
[28] B.D. Cullity, Elements of X-ray diffraction, Am. J. Phys. 25 (1956) 394.
[29] V.D. Hodoroaba, Energy-dispersive X-ray spectroscopy, in: Characterization of Nanoparticles, Elsevier, 2020, pp. 397–417.
[30] M. Manikandan, K.S. Kumar, C. Venkateswaran, Mn doping instigated multiferroicity and magneto-dielectric coupling in $KNbO_3$, J. Appl. Phys. 118 (23) (2015), 234105.
[31] C. Ren, C. Tan, L. Gong, M. Tang, M. Liao, J. Wang, Highly transparent, all-oxide, heteroepitaxy ferroelectric thin film for flexible electronic devices, Appl. Surf. Sci. 458 (2018) 540–545.
[32] A. Quader, G.M. Mustafa, S.K. Abbas, H. Ahmad, S. Riaz, S. Naseem, S. Atiq, Efficient energy storage and fast switching capabilities in Nd-substituted $La_2Sn_2O_7$ pyrochlores, Chem. Eng. J. 396 (2020), 125198.
[33] M. Barthélémy, A. Bibes, Multiferroics: towards a magnetoelectric memory, Nat. Mater. 7 (6) (2008) 425–426.
[34] W. Xia, J. Zhou, T. Hu, P. Ren, G. Zhu, Y. Yin, Z. Zhang, Enhanced magnetoelectric coefficient and interfacial compatibility by constructing a three-phase CFO@ BT@ PDA/P (VDF-TrFE) core-shell nanocomposite, Compos. Part A Appl. Sci. Manuf. 131 (2020), 105805.
[35] R. Cai, V.A. Antohe, Z. Hu, B. Nysten, L. Piraux, A.M. Jonas, Multiferroic nanopatterned hybrid material with room-temperature magnetic switching of the electric polarization, Adv. Mater. 29 (6) (2017), 1604604.
[36] M.M.S. He, Study of structural, electronic and magnetic properties of transition-metal perovskite oxides $SrMO_3$ (M= Mn and Co) by XRD and DFT techniques, Dig. J. Nanomater. Biostructures 11 (4) (2016) 1383–1396.
[37] M. Hoffmann, V.S. Borisov, S. Ostanin, I. Mertig, W. Hergert, A. Ernst, Magnetic properties of defect-free and oxygen-deficient cubic $SrCoO_{3-\delta}$, Phys. Rev. B 92 (9) (2015), 094427.